International Journal of Energy and Environmental Engineering (2019) 10:287–305
https://doi.org/10.1007/s40095-019-0306-z

ORIGINAL RESEARCH

Fixed-frequency implementation of sliding-mode controllers for photovoltaic systems

Daniel González Montoya[1] · **Paula Andrea Ortiz Valencia**[1] · **Carlos Andrés Ramos-Paja**[2]

Received: 6 December 2018 / Accepted: 22 April 2019 / Published online: 3 May 2019

Abstract

Traditional implementation of sliding-mode controllers, based on hysteresis comparators, exhibits variable switching frequency. Such a condition makes it difficult to select the semiconductor devices, design the passive elements of dc/dc converters, and design the sensing filters usually adopted for removing the switching noise from currents and voltages. Those problems are always present in photovoltaic systems based on variable-frequency sliding-mode controllers. Therefore, this paper proposes an implementation methodology for sliding-mode controllers providing constant switching frequency, which is aimed for grid-connected photovoltaic applications. The proposed solution does not compromise the power production of the PV system, hence it provides the same PV power in comparison with the classical variable-frequency implementation. Finally, the performance and correct operation of the fixed-frequency implementation are demonstrated using both simulation and experimental results.

Keywords Photovoltaic systems · Sliding-mode control · Adaptive hysteresis band · Fixed frequency

Abbreviations

v_{pv}	PV array voltage (V)
i_{pv}	PV array current (A)
p_{pv}	PV array power (W)
L	Inductor value (H)
C_{in}	Input capacitor value (F)
C_b	Output capacitor value (F)
i_L	Inductor current (A)
v_b	Load voltage (V)
u	MOSFET digital signal
d	Duty cycle
i_{sc}	PV short-circuit current (A)
B	Diode saturation current (A)
A	Inverse of the thermal voltage (V^{-1})
T_a	MPPT disturbance period (s)
Δv_{pv}	MPPT disturbance magnitude (V)
Ψ	Switching function
Φ	Sliding surface
h	Width of the hysteresis band
T_{sw}	Switching period (s)
F_{sw}	Switching frequency (Hz)
Ψ_L	Inductor current switching function (A)
i_{ref}	Inductor current reference (A)
R_{MPP}	PV array differential resistance (Ω)
Ψ_V	PV voltage switching function (V)
v_{ref}	PV voltage reference (V)
K_1, K_2	Dynamic gains
R_s	Shunt resistance (Ω)

Introduction

The solar irradiance is a renewable and clean energy source that is attracting interest due to its low environmental impact, high sustainability and availability at almost any place [1]. Hence, photovoltaic (PV) generators have become a stronger option to address the continuous increment of the power demand and to support the initiative of reducing the use of fossil fuels [1]. Moreover, the PV systems could be used to provide ancillary services for supporting the grid [2, 3] but, at the same time, the introduction of PV systems generates

---

✉ Daniel González Montoya
danielgonzalez@itm.edu.co

Paula Andrea Ortiz Valencia
paulaortiz@itm.edu.co

Carlos Andrés Ramos-Paja
caramosp@unal.edu.co

[1] Departamento de Electrónica y Telecomunicaciones, Instituto Tecnológico Metropolitano, Medellín, Colombia

[2] Facultad de Minas, Universidad Nacional de Colombia, Medellín, Colombia

changes in the power-system dynamics that must be modeled to avoid instabilities [4]. One of the challenges in controlling PV systems concerns the variability of the power production, which is mainly caused by the variation on the irradiance level, or by partial shading produced by surrounding objects [5], causing the activation of bypass diodes. The most commonly adopted solutions to face the partial shading problem are: reconfiguration of the electrical connections forming the PV array [6], global maximum power point tracking techniques [7] and distributed maximum power point (DMPPT) architectures [8]. The DMPPT architectures are the solutions that produce the highest power, since bypass diodes are not activated. Therefore, micro-inverters have been developed to isolate one PV panel from the others, forming in this way a DMPPT architecture. Such a solution improves the power production of small PV plants by reducing the effect of partial shading conditions [7], but introducing the same problems of any grid-connected PV system.

A typical grid-connected PV system is composed by a PV array, a dc/dc converter to transform the power provided by the PV source, a controller to mitigate disturbances, and a grid-connected inverter as it is illustrated in Fig. 1. The PV array exhibits a non-linear behavior that changes significantly with the operating conditions (irradiance, temperature, and voltage at the array terminals), which makes difficult to predict the optimal PV voltage and current to guarantee the maximum power production [9, 10].

The design of a controller capable of rejecting disturbances occurring at both the photovoltaic array and the load represent one of the main challenges in the implementation of this kind of systems [11, 12]. Usually, grid-connected PV systems are controlled by a cascade connection of a maximum power point tracking (MPPT) algorithm and a PV voltage controller, where linear controllers (PI, PID or lead–lag) are a widely adopted alternative [9, 11–13]. Moreover, the Perturb and Observe (P&O) is a widely adopted MPPT algorithm, which provides a satisfactory trade-off between complexity and performance for the optimization of the operating point of renewable power sources [14].

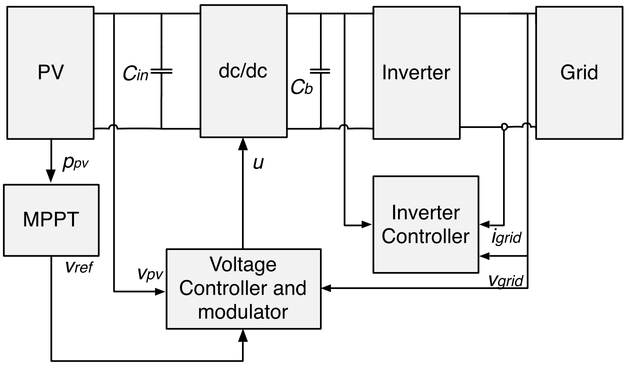

Fig. 1 Scheme of a classical grid-connected PV system

To guarantee a correct tracking of the reference generated by the MPPT algorithm, and to mitigate the disturbances in both the load and the environmental conditions, the linear controllers are commonly designed from the model of the PV system linearized around a given specific operating point, e.g., the maximum power point (MPP) at the lowest irradiance condition [9, 10]. Thus, to guarantee the same performance in all the operation ranges it is necessary to design non-linear controllers based on non-linearized models. In this way, the sliding-mode control (SMC) is an effective non-linear approach with several advantages: robustness against parametric tolerances, global stability, and a binary control signal matching the requirements of the dc/dc converter [9]. Therefore, the regulation of grid-connected PV system using SMC has been extensively addressed in the literature as reported in [9, 15–20]. However, those solutions provide the classical implementation based on a variable-switching frequency that depends on the dc/dc converter parameters and on the operating conditions imposed by both the environment and load. Such a variable-switching frequency is a major problem for practical circuits based on SMC ([15, 21]) due to the operational restrictions imposed to the semiconductor devices, making the implementation of filters required for measuring the signals used for processing both the controller and MPPT algorithm also difficult [22]. Moreover, some SMC implementations use digital devices [23], hence the switching frequency cannot exceed the sampling frequency of the analog-to-digital-converters (ADC) used to measure the PV voltage and current [24]. Therefore, a constant switching frequency is desired to simplify the implementation of SMC for PV systems: accurate filters design, correct selection of both ADC and control microprocessors, precise selection of the semiconductors depending of both Turn-ON and Turn-OFF times, among other advantages that will decrease the implementation cost and complexity.

This topic, in the context of dc/dc converters, was addressed in [21] using the equivalent control value of the SMC as duty cycle. This approach results in a duty cycle regulation following the theoretical sliding-mode surface provided to a traditional PWM circuit. Another approach was proposed in [25], which reports a fixed-frequency SMC to improve the dynamic response of a single-phase inverter subjected to a sudden fluctuation of the load. This solution uses a flip-flop to generate the control signal with an additional constant frequency clock to impose a constant Turn-ON time. However, those solutions were not analyzed considering the PV source.

This paper proposes a methodology for implementing sliding-mode controllers with constant switching frequency for the Maximum Power Point Tracking of PV systems.

The proposed method is aimed at implementing first-order sliding-mode controllers due to the large amount of those solutions reported in literature [9, 15, 16, 19, 20]. The paper is organized as follows: Section 2 presents the background of the proposed design procedure, then Sect. 3 describes the proposed methodology based on an adaptive hysteresis. Section 4 illustrates the application of the proposed solution to SMCs reported in literature; this section demonstrates the performance of the proposed implementation method using detailed simulations. Moreover, Sect. 5 provides experimental verifications of the fixed-frequency provided by the proposed solution. Finally, the conclusions close the paper.

Background of the proposed solution

The solution proposed in this paper is aimed at implementing sliding mode controllers, operating at fixed frequency, to regulate the PV voltage and to mitigate the low frequency voltage oscillations caused at the bulk capacitor C_b, reported in Fig. 2, by the inverter operation in grid-connected PV systems [19].

The PV system depicted in Fig. 2 is based on a boost converter, which is widely adopted to develop grid-connected PV systems because it provides a satisfactory trade-off between simplicity, cost and voltage-boosting factor [26]. Therefore, the boost converter is the topology adopted in this paper for the dc/dc stage of the grid-connected PV system. The simplified circuital scheme of the PV system, presented in Fig. 2, includes a voltage source modeling the dc-link and the grid-connected inverter. Such a voltage source model is an accurate representation because the dc/ac stage regulates the dc-link voltage (C_b capacitor voltage) as it is reported in [9, 11, 26].

Equations (1) and (2) provide the dynamic model of the PV system [26], where v_{pv} and i_{pv} represent the voltage and the current of the PV array, respectively, i_L represents the inductor current, v_b is the load voltage, while L and C_{in} represent the inductor and input capacitor values. Moreover, u represents the control signal that defines the MOSFET and diode status: $u = 0$ open the MOSFET (close the diode) and $u = 1$ close the MOSFET (open the diode).

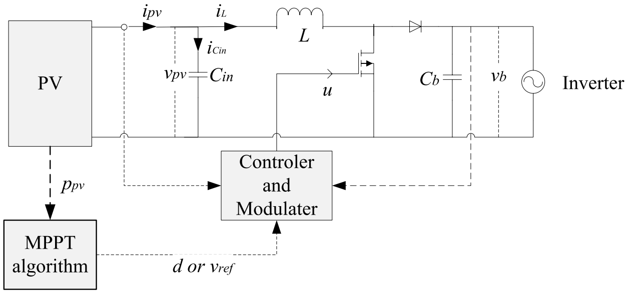

Fig. 2 Two-stage grid-connected PV system

$$\frac{\mathrm{d}i_L}{\mathrm{d}t} = \frac{v_{\mathrm{pv}} - v_{\mathrm{b}} \cdot (1-u)}{L} \tag{1}$$

$$\frac{\mathrm{d}v_{\mathrm{pv}}}{\mathrm{d}t} = \frac{i_{\mathrm{pv}} - i_L}{C_{\mathrm{in}}} \tag{2}$$

The PV array is modeled using the ideal single diode model (ISDM) reported in [9], which is extensively used to design controllers due to the satisfactory balance between accuracy and simplicity [26]. From that model, the PV current i_{pv} is given in (3). In the ISDM i_{sc} represents the short-circuit current, which is almost proportional to the irradiance, B is the diode saturation current and A represents the inverse of the thermal voltage, which depends on the temperature [26]. Those parameters can be calculated from datasheet values or experimental measurements [26], hence the model can be updated depending on the changes occurring on the environmental conditions.

$$i_{\mathrm{pv}} = i_{\mathrm{sc}} - B \cdot \left(e^{A \cdot v_{\mathrm{pv}}} - 1\right) \tag{3}$$

Figure 2 also depicts the connection between the MPPT algorithm and the main controller. This paper adopts the P&O algorithm due to its efficiency and simplicity. The operation principle of the P&O algorithm is the following: the PV voltage is perturbed in the direction that increases the PV power, hence if the power is decreased, the PV voltage is perturbed in the opposite direction [14]. This behavior enables to detect the optimal PV voltage that maximizes the power production. The flowchart of the P&O algorithm is given in Fig. 3, in which k and $k-1$ represent the present and previous processing cycles of the algorithm, respectively, which are executed each disturbance period T_a. The variable *Sign* codifies the direction in which the PV voltage is perturbed (Sign = 1 for increment and Sign = − 1 for decrement), while term Δv_{pv} corresponds to the disturbance magnitude that will be introduced into the PV voltage. This flow-chart put into evidence the discrete nature of the P&O algorithm, hence it must be implemented using a digital microprocessor.

There are reported in literature multiple SMC aimed at regulating the PV voltage to follow the reference generated by a P&O algorithm, i.e., following the structure given in Fig. 2. From those solutions, three approaches with different relations between complexity and performance have been selected to illustrate the application and usefulness of the proposed fixed-frequency implementation technique. The selected SMCs are: first, the approach published in [15], which is based on the sliding-mode control of the inductor current, it requiring simple analytical expressions; however,

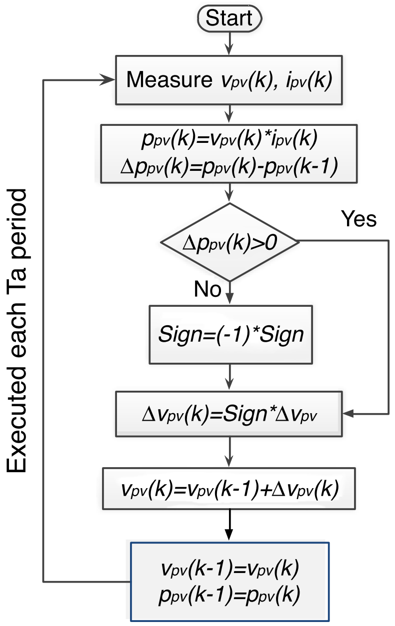

Fig. 3 P&O flowchart

the design of an additional cascade voltage control requires an equivalent model parameterized in a given operating point. The second approach, published in [16], is based on the sliding-mode control of the input capacitor current, which requires more complex analytical expressions but the resulting cascade voltage control is independent of the operating point. The third approach, published in [9], is based on a sliding surface depending on both the input capacitor current and PV voltage, which avoids the requirement of cascade voltage controllers. This feature increases the bandwidth of the controller at the expense of much complicated mathematical analyses. In conclusion, applying the proposed fixed-frequency implementation technique to those control approaches will put into evidence the practical usefulness of the solution.

The following subsection describes the basic tools required to analyze sliding-mode controllers, which are used to introduce the proposed fixed-frequency implementation technique. Moreover, Sects 2.2, 2.3 and 2.4 provide the main equations of each selected case, which are required to apply the implementation technique.

Basic concepts of sliding-mode control

Sliding-mode controllers are a special type of variable structure systems, in which the state of the system dynamics is attracted to a desired sliding surface defined in the state-space. When certain conditions are fulfilled, the state of the system "slides" into the surface, it remaining (ideally) insensitive to variations in the parameters of the plant and to external disturbances. Therefore, the main goals of a SMC are to force the system trajectories to reach a given sliding surface Φ and to force the system to keep trapped into Φ. In those conditions, the behavior of the closed-loop system is determined by the equations describing the sliding surface $\Phi = \{\Psi = 0\}$, where Ψ is the sliding function. Sira-Ramirez demonstrated in [27] the three conditions that must be fulfilled to ensure the existence of the sliding mode, i.e., ensure the operation into Φ: transversality, reachability, and equivalent control.

Transversality condition

The transversality condition, given in (4), evaluates the presence of the manipulated variable u into the switching function derivative [22], which is required to modify the system dynamics. Therefore, if (4) is not fulfilled, the SMC will not be able to affect the system behavior.

$$\frac{\mathrm{d}}{\mathrm{d}u}\left(\frac{\mathrm{d}\Psi}{\mathrm{d}t}\right) \neq 0 \tag{4}$$

Reachability conditions

The reachability conditions analyze the ability of the system to reach the desired state $\Psi = 0$. The concept is the following: when the system is operating under the surface, i.e., $\Psi < 0$ ($\Psi \to 0^-$ near the surface), the derivative of the switching function must be positive to increase the value of Ψ. Similarly, when the system is operating over the surface, i.e., $\Psi > 0$ ($\Psi \to 0^+$ near the surface), the derivative of the switching function must be negative to decrease the value of Ψ. Those conditions are formalized as follow:

$$\lim_{\Psi \to 0^-} \frac{\mathrm{d}\Psi}{\mathrm{d}t} > 0 \tag{5}$$

$$\lim_{\Psi \to 0^+} \frac{\mathrm{d}\Psi}{\mathrm{d}t} < 0 \tag{6}$$

If those expressions are fulfilled the system will converge to the surface, hence the system will be controller according to $\Phi = \{\Psi = 0\}$.

However, the sign of the switching function derivative must be also analyzed to provide practical tests: if the transversality (4) has a positive sign, it means a positive value of u imposes a positive derivative to the surface Ψ, i.e., $\left\{\frac{\mathrm{d}}{\mathrm{d}u}\left(\frac{\mathrm{d}\Psi}{\mathrm{d}t}\right) > 0 \wedge u = 1\right\} \rightarrow \frac{\mathrm{d}\Psi}{\mathrm{d}t} > 0$. Instead, if the transversality has a negative sign, it means a positive value of u imposes a negative derivative to Ψ, i.e., $\left\{\frac{\mathrm{d}}{\mathrm{d}u}\left(\frac{\mathrm{d}\Psi}{\mathrm{d}t}\right) < 0 \wedge u = 1\right\} \rightarrow \frac{\mathrm{d}\Psi}{\mathrm{d}t} < 0$. Those analyses lead to the following practical reachability conditions:

$$\frac{\mathrm{d}}{\mathrm{d}u}\left(\frac{\mathrm{d}\Psi}{\mathrm{d}t}\right) > 0 \Rightarrow \left\{ \begin{array}{l} \lim\limits_{\Psi \to 0^-} \left.\frac{\mathrm{d}\Psi}{\mathrm{d}t}\right|_{u=1} > 0 \\ \\ \lim\limits_{\Psi \to 0^+} \left.\frac{\mathrm{d}\Psi}{\mathrm{d}t}\right|_{u=0} < 0 \end{array} \right\} \tag{7}$$

$$\frac{\mathrm{d}}{\mathrm{d}u}\left(\frac{\mathrm{d}\Psi}{\mathrm{d}t}\right) < 0 \Rightarrow \left\{ \begin{array}{l} \lim\limits_{\Psi \to 0^-} \left.\frac{\mathrm{d}\Psi}{\mathrm{d}t}\right|_{u=0} > 0 \\ \\ \lim\limits_{\Psi \to 0^+} \left.\frac{\mathrm{d}\Psi}{\mathrm{d}t}\right|_{u=1} < 0 \end{array} \right\} \tag{8}$$

Expressions (7) and (8) define the control law of the SMC [9] depending on the transversality value exhibited by the system. Moreover, fulfilling both the transversality and reachability conditions also guarantees that the trajectory of the system will be parallel to the surface as it is demonstrated in [27], hence the following closed-loop conditions hold:

$$\left\{\Psi = 0 \wedge \frac{\mathrm{d}\Psi}{\mathrm{d}t} = 0\right\} \tag{9}$$

However, implementing the control laws given in (7) or (8) requires an infinite switching frequency, which is impossible to obtain with real semiconductor devices. Therefore, an hysteresis band is added to the control law to limit the switching frequency [9] as it is depicted in Fig. 4. In this way, the switching frequency is defined by the values of the switching function Ψ derivatives (both positive and negative) and by the size of the band. Fig. 4 illustrates such a condition, where h is the width of the hysteresis band, therefore the band limits are $\left\{-\frac{h}{2}, \frac{h}{2}\right\}$. But, due to the constant value of the hysteresis band, the switching frequency changes when the derivatives of Ψ change, which occurs due to disturbances in the operating conditions as it is illustrated in Fig. 4. This concept will be used in Sect. 3 to propose the new fixed-frequency implementation technique.

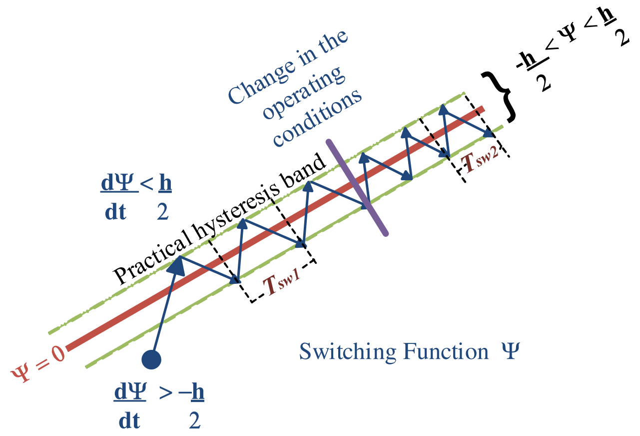

Fig. 4 Basic concept of SMC operation

Equivalent control condition

The equivalent control condition requires that the average value u_{eq} of the control variable u be constrained within the practical operation range [27]. For dc/dc converters the limits of u are 0 (MOSFET open) and 1 (MOSFET close), moreover in dc/dc converters the average value of u is equal to the duty cycle d. Therefore, fulfilling the equivalent control condition guarantees the duty cycle of the converter is not saturated. The formal expression of the equivalent control condition is given in (10), in which T_{sw} represents the switching period.

$$0 < u_{eq} = \frac{1}{T_{\mathrm{sw}}} \cdot \int_0^{T_{\mathrm{sw}}} u \, \mathrm{d}t < 1 \tag{10}$$

Finally, Sira-Ramirez demonstrated in [27] that any system fulfilling the reachability conditions also fulfills the equivalent control condition.

Sliding-mode control of the inductor current

The solution proposed in [15], is based on the sliding-mode control of the inductor current to provide global stability. The solution considers a cascade control formed by a P&O algorithm to detect the optimal voltage reference, a linear voltage regulator G_{cc} providing the current reference to reach the desired optimal voltage, and the SMC regulating the inductor current. Figure 5 shows the circuit scheme and illustrates the control structure.

The switching function Ψ_L and sliding surface Φ_L used to design the SMC are given in (11).

$$\Psi_{\mathrm{L}} = i_{\mathrm{L}} - i_{\mathrm{ref}} \wedge \Phi_{\mathrm{L}} = \{\Psi_{\mathrm{L}} = 0\} \tag{11}$$

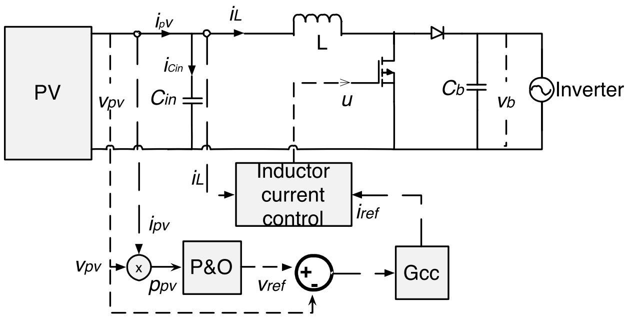

Fig. 5 Schema system based on inductor current control

The evaluation of the transversality condition (4) is reported in (12), which demonstrates that (11) is suitable to implement a SMC because both v_b and L are positive values, i.e., equation (12) is different from zero.

$$\frac{d}{du}\left(\frac{d\Psi_L}{dt}\right) = \frac{v_b}{L} > 0 \tag{12}$$

Since the transversality value is positive, the reachability conditions given in (7) must be tested:

$$\frac{d\Psi_{L,up}}{dt} = \lim_{\Psi_L \to 0^-} \frac{d\Psi_L}{dt}\bigg|_{u=1} = \frac{v_{pv}}{L} > 0 \tag{13}$$

$$\frac{d\Psi_{L,dw}}{dt} = \lim_{\Psi_L \to 0^+} \frac{d\Psi_L}{dt}\bigg|_{u=0} = \frac{v_{pv} - v_b}{L} < 0 \tag{14}$$

Such expressions guarantee the global stability of the closed-loop system since $v_b > v_{pv} > 0$, which is a basic operation condition of the boost converter. In (13) and (14) the subindexes up and dw have been added to identify the positive and negative derivatives of Ψ_L, respectively; this nomenclature will be used in Sect. 3 to describe the new fixed-frequency implementation technique. Finally, the equivalent control condition is granted because both reachability conditions (13) and (14) are fulfilled.

The action of the SMC produces an equivalent closed-loop dynamic that must be modeled to design the voltage controller G_{cc}. Replacing the voltage differential equation (2) and the sliding-mode equation (11) into the closed-loop conditions imposed by the SMC (9), in Laplace domain, leads to the following equivalent dynamic:

$$\frac{V_{pv}(s)}{I_{ref}(s)} = \frac{-R_{MPP}}{R_{MPP} \cdot C_{in} \cdot s + 1} \tag{15}$$

In such an expression $R_{MPP} = \left|\frac{\partial v_{pv}}{\partial i_{pv}}\right|$ represents the differential resistance of the PV array [14], which depends on the irradiance, temperature and operating point. Expression (15) put into evidence the global stability provided by the SMC because equivalent pole $s = -1/\left(R_{MPP} \cdot C_{i_n}\right)$ is always negative. Moreover, since v_b is not present in the equivalent dynamic (15), any disturbance in the dc-link C_b is mitigated. However, the settling time of the PV voltage in (15) depends on R_{MPP}, hence the transfer function must be parameterized at the most critical case, i.e., the one with the longer settling time, which corresponds to the lower irradiation expected as it is reported in [14].

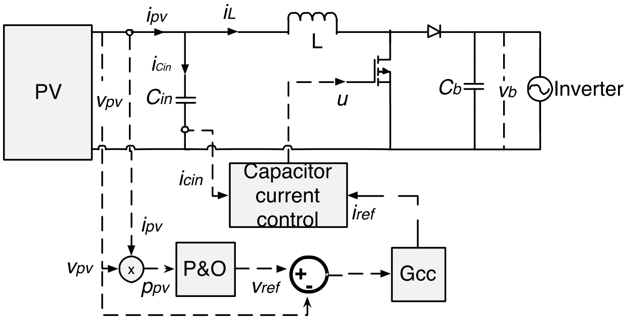

Fig. 6 Schema system based on Capacitor current control

Sliding-mode control of the input capacitor current

The second case to be analyzed is based on the regulation of the input capacitor current $i_{C_{in}}$ published in [16]. This SMC improvement provides both global stability and constant settling time to the PV system. Moreover, the measurement of the input capacitor current is simpler, in comparison with the measurement of the inductor current, due to both the ground connection of C_{in} and the zero dc component of the capacitor current [16]. The control structure, depicted in Fig. 6, is similar to the one described in the previous subsection, but in this case the switching function Ψ_C and the sliding surface Φ_C are given in (16).

$$\Psi_C = i_{C_{in}} - i_{ref} \wedge \Phi_C = \{\Psi_C = 0\} \tag{16}$$

Deriving Ψ_C from (16), and taking into account that $i_{C_{in}} = i_{pv} - i_L$, enables to calculate the explicit derivative of Ψ_C:

$$\frac{d\Psi_C}{dt} = \frac{di_{pv}}{dt} - \frac{v_{pv} - v_b \cdot (1-u)}{L} \tag{17}$$

The evaluation of the transversality condition is reported in (18), which imposes the reachability conditions given in (8).

$$\frac{d}{du}\left(\frac{d\Psi}{dt}\right) = \frac{-v_b}{L} < 0 \tag{18}$$

The evaluation of those reachability conditions is reported in (19) and (20), which impose the dynamic restriction given in (21) to the PV current.

$$\frac{d\Psi_{C,up}}{dt} = \lim_{\Psi_C \to 0^-} \frac{d\Psi_C}{dt}\bigg|_{u=0} = \frac{d_{ipv}}{dt} - \frac{v_{pv} - v_b}{L} > 0 \tag{19}$$

$$\frac{d\Psi_{C,dw}}{dt} = \lim_{\Psi_C \to 0^+} \frac{d\Psi_C}{dt}\bigg|_{u=1} = \frac{d_{ipv}}{dt} - \frac{v_{pv}}{L} < 0 \tag{20}$$

$$\frac{v_{pv} - v_b}{L} < \frac{di_{pv}}{dt} < \frac{v_{pv}}{L} \tag{21}$$

In practice, limitation (21) informs that the PV current could be changed with a maximum speed imposed by the inductor current, i.e., the maximum derivative of the PV current must be lower than the maximum derivative of the inductor current, similarly the minimum derivative of the PV current must be higher than the minimum derivative of the inductor current. Thus, the inequality given in (21) reveals that the maximum irradiance variation that can be tracked without losing the sliding-mode control. For example, considering $L = 330\ \mu\mathrm{H}$, $v_b = 24\ \mathrm{V}$ and $v_{pv} = 18\ \mathrm{V}$, the PV current derivative must be constrained to $-18.2\ \mathrm{A/ms} < \frac{di_{pv}}{dt} < 54.5\ \mathrm{A/ms}$, which approximated correspond [26] to $-3868.5\ \mathrm{W}/\left(\mathrm{m}^2\ \mathrm{ms}\right) < \frac{dS}{dt} < 11605.4\ \mathrm{W}/\left(\mathrm{m}^2\ \mathrm{ms}\right)$, i.e., very high irradiance derivative restrictions difficult to violate on practice. Therefore, this solution provides global stability in any practical case.

The equivalent closed-loop dynamics of this case, in Laplace domain, are reported in (22). Therefore, any disturbance injected in v_b is mitigated. Moreover, the dynamic behavior of (22) does not depend on the operating point, hence a cascade voltage controller designed with (22) is able to provide the same performance (settling time and damping ratio) at any operation condition.

$$\frac{V_{pv}(s)}{I_{ref}(s)} = \frac{-1}{C_{in} \cdot s} \tag{22}$$

Sliding-mode control of the PV voltage

The previous solutions have a voltage-current cascade structure, which reduces the bandwidth of the PV voltage as it is explained in [9]. To remove that cascade control, the solution reported in [9], and illustrated in Fig. 7, proposes a single SMC based on both the input capacitor current and PV voltage error. For this case, the switching function Ψ_V and sliding surface Φ_V are given in (23), where K_1 and K_2 are constants used to define the dynamic behavior of the PV system.

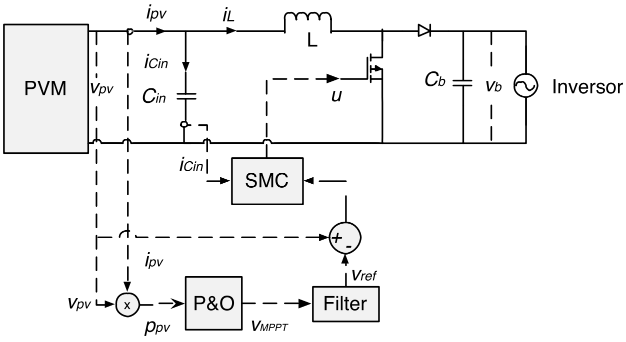

Fig. 7 Complete PV system including the reference filter

$$\Psi_V = (v_{pv} - v_{ref}) \cdot K_1 + i_{Cin} \cdot K_2 \quad \wedge \quad \Phi_V = \{\Psi_V = 0\} \tag{23}$$

The transversality, reachability, and equivalent control conditions are extensively demonstrated in [9]. A summary of those analytical proofs is the following:

- The transversality condition, given in (24), imposes a first constraint that must be fulfilled by K_2 to ensure controlability. Moreover, the design process developed in [9] imposes a K_2 value that ensures a positive transversality condition.

$$\frac{d}{du}\left(\frac{d\Psi_V}{dt}\right) = \frac{-(K_2 \cdot v_b)}{L} \neq 0 \tag{24}$$

- The reachability conditions imposed by a positive value of the transversality are given in (7). Deriving (23), and replacing such an expression in (7) leads to constraints (25) and (26), where the intermediate variable y is given in (27).

$$\begin{aligned}\lim_{\Psi \to 0^-} \left.\frac{d\Psi_V}{dt}\right|_{u=1} =& \frac{dv_{pv}}{dt} \cdot (K_1 + K_2 \cdot y) - K_1 \cdot \frac{dv_{ref}}{dt} \\ &+ K_2 \cdot \frac{di_{SC}}{dt} - K_2 \cdot \frac{v_{pv}}{L} > 0\end{aligned} \tag{25}$$

$$\begin{aligned}\lim_{\Psi \to 0^+} \left.\frac{d\Psi_V}{dt}\right|_{u=0} =& \frac{dv_{pv}}{dt} \cdot (K_1 + K_2 \cdot y) - K_1 \cdot \frac{dv_{ref}}{dt} \\ &+ K_2 \cdot \frac{di_{SC}}{dt} - \frac{K_2 \cdot v_{pv} - v_b}{L} < 0\end{aligned} \tag{26}$$

$$y = -B \cdot A \cdot \left(e^{A \cdot v_{pv}}\right) \tag{27}$$

Expressions (25) and (26) impose two additional restrictions for K_1 and K_2 that must be fulfilled to ensure global stability. Such restrictions depend, first, on the maximum irradiance derivative expected, which in this case is represented in terms of the short-circuit current derivative $\frac{di_{SC}}{dt}$, this leading to a practical analysis similar to the one performed for the previous case. The restrictions also depend on the derivative of the reference signal $\frac{dv_{ref}}{dt}$, which is limited by the low-pass filter introduced between the P&O algorithm and the SMC as it is illustrated in Fig. 7.

- The procedure to calculate K_1 and K_2 values that simultaneously fulfill the constrains imposed by (24), (25) and (26) is reported in [9]. Therefore, such a design procedure enables to guarantee global stability.

The design procedure reported in [9] also takes into account the effect of the low-pass filter into the dynamics of the PV voltage, providing values for K_1 and K_2 that ensures a null overshoot and a constant settling time for any operation condition. Finally, due to the larger bandwidth provided by the direct PV voltage control, in comparison with the current-voltage cascade solutions, this SMC provides a shorter settling time, i.e., a faster reference tracking, but at the expense of more complicated mathematical analysis and design equations.

Fixed-frequency implementation technique based on adaptive hysteresis

Section 2.1.2 analyzed the two conditions causing the switching frequency variation in presence of disturbances: the hysteresis band is constant but the derivatives of the switching function change, hence the time required by the switching function to travel between the limits of the hysteresis band also changes. Since the switching period T_{sw} depends on the time required by the switching function to travel between the limits of the hysteresis band, the switching frequency F_{sw} changes.

From Fig. 4 the practical control law is extracted, including the effect of the hysteresis band, which modifies the theoretical reachability conditions (5) and (6) as follow:

$$\lim_{\Psi \to \frac{-h}{2}} \frac{\mathrm{d}\Psi}{\mathrm{d}t} > 0 \tag{28}$$

$$\lim_{\Psi \to \frac{h}{2}} \frac{\mathrm{d}\Psi}{\mathrm{d}t} < 0 \tag{29}$$

Combining (28) and (29) with the reachability conditions for a positive transversality value, given in (7), leads to the practical control law for systems with a positive transversality value given in (30).

$$\frac{\mathrm{d}}{\mathrm{d}u}\left(\frac{\mathrm{d}\Psi}{\mathrm{d}t}\right) > 0 \Rightarrow \left\{ \begin{matrix} \text{if} \quad \Psi <= \dfrac{-h}{2} \quad \text{set} \quad u = 1 \\ \text{if} \quad \Psi >= \dfrac{h}{2} \quad \text{set} \quad u = 0 \end{matrix} \right\} \tag{30}$$

Similarly, combining (28) and (29) with (8) leads to the practical control law for systems with a negative transversality value given in (31).

$$\frac{\mathrm{d}}{\mathrm{d}u}\left(\frac{\mathrm{d}\Psi}{\mathrm{d}t}\right) < 0 \Rightarrow \left\{ \begin{matrix} \text{if} \quad \Psi <= \dfrac{-h}{2} \quad \text{set} \quad u = 0 \\ \text{if} \quad \Psi >= \dfrac{h}{2} \quad \text{set} \quad u = 1 \end{matrix} \right\} \tag{31}$$

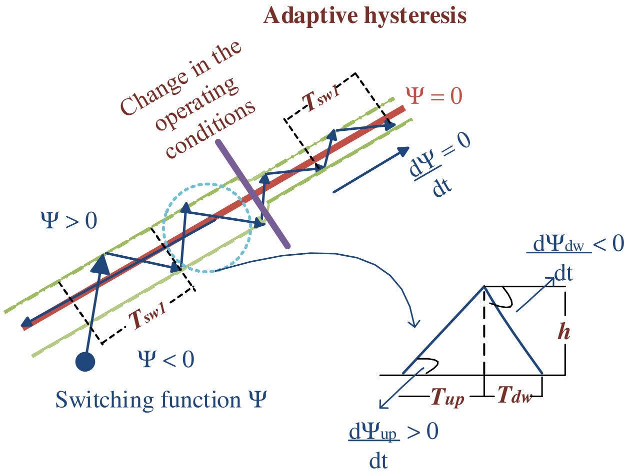

Fig. 8 SMC operation for first order with adaptive hysteresis band

To avoid the frequency variation due to changes in the operating point, the width h of the hysteresis band must be adapted: if the derivative of the switching function increases, h must be increased to keep constant the time needed to reach the band limit; similarly, if the derivative of the switching function decreases, h must be decreased. This concept is illustrated in Fig. 8, in which the hysteresis band is reduced to keep the switching frequency constant.

The implementation technique proposed in this paper is aimed for first-order sliding surfaces, hence the switching function must have first-order terms only. This decision is

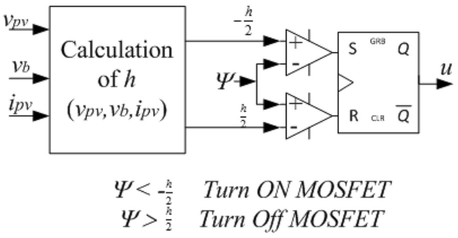

Fig. 9 Practical implementation for SMC with positive transversality values

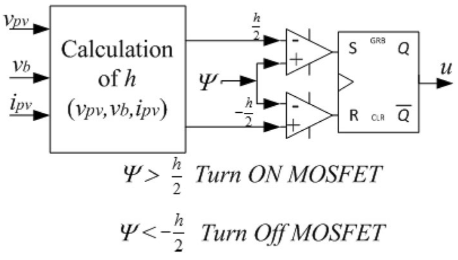

Fig. 10 Practical implementation for SMC with negative transversality values

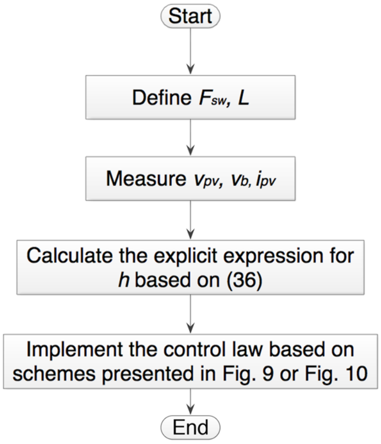

Fig. 11 Flow chart of the proposed solution

based on the large amount of first-order SMC designed for PV systems reported in literature [9, 15, 16, 18]. The first-order condition ensures a triangular waveform of the switching function, as it is depicted in both Figs. 4 and 8, which enables a fast calculation of the time required by the switching function to reach the hysteresis band limits.

Figure 8 also illustrates the method used to calculate the time t_{up} required by the switching function Ψ to travel from the lower band limit to the upper band limit, hence traveling a distance equal to the band width h. Similarly, the time required by Ψ to travel from the upper limit to the lower limit is t_{dw}. From Fig. 8 it is concluded that t_{up} depends on the positive derivative of the switching function $\frac{\mathrm{d}\Psi_{\mathrm{up}}}{\mathrm{d}t} > 0$ as follows:

$$t_{\mathrm{up}} = \frac{h}{\frac{\mathrm{d}\Psi_{\mathrm{up}}}{\mathrm{d}t}} \tag{32}$$

From the figure it is also concluded that t_{dw} depends on the negative derivative of the switching function $\frac{d\Psi_{\mathrm{dw}}}{\mathrm{d}t} < 0$ as it is given in (33). In that expression the derivative is negative, hence the vectorial quantity changed in Ψ is negative $(-h)$.

$$t_{\mathrm{dw}} = \frac{-h}{\frac{d\Psi_{\mathrm{dw}}}{\mathrm{d}t}} \tag{33}$$

Figure 8 also shows that the switching period T_{sw} corresponds to the sum of both t_{up} and t_{dw}, which leads to the following expression for the switching frequency F_{sw}:

$$F_{\mathrm{sw}} = \frac{1}{T_{\mathrm{sw}}} = \frac{1}{t_{\mathrm{up}} + t_{\mathrm{dw}}} \tag{34}$$

Replacing (32) and (33) into (34) leads to:

$$F_{sw} = \frac{1}{\frac{h}{\frac{\mathrm{d}\Psi_{\mathrm{up}}}{dt}} - \frac{h}{\frac{\mathrm{d}\Psi_{dw}}{dt}}} \tag{35}$$

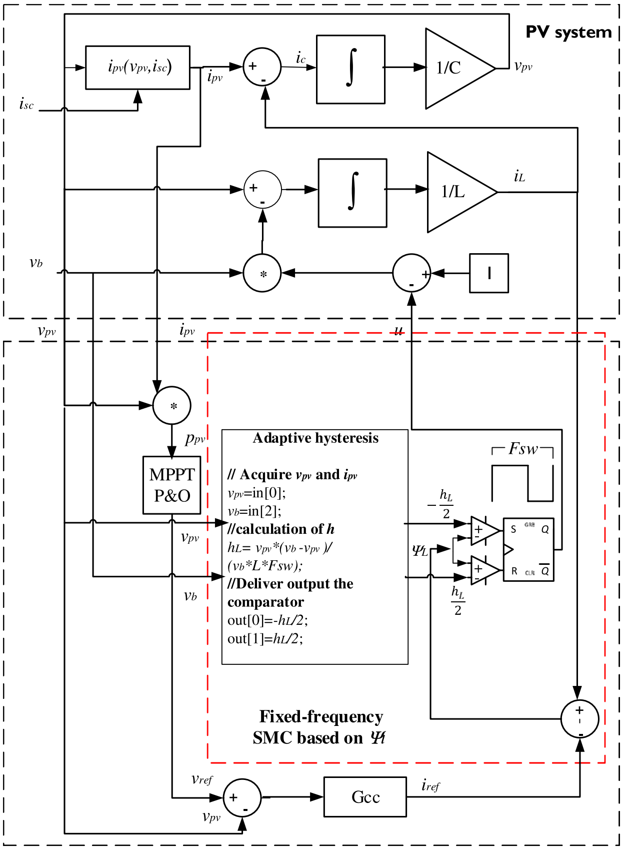

```
Adaptive hysteresis

// Acquire vpv and ipv
vpv=in[0];
vb=in[2];
//calculation of h
hL= vpv*(vb -vpv )/
(vb*L*Fsw);
//Deliver output the
comparator
out[0]=-hL/2;
out[1]=hL/2;
```

Fig. 12 Block diagram of the SMC based on Ψ_L

Finally, the expression for adapting h to ensure a fixed switching frequency F_{sw} is given in (36). It must be highlighted that such an expression depends on the switching function derivatives, therefore the SMC to be implemented must be analyzed as described in the examples reported in Sect. 2. In any case, those analyses are required to demonstrate global stability and to design the dynamic behavior of the closed-loop system.

$$h\left(v_{\mathrm{pv}}, i_{\mathrm{pv}}, v_{\mathrm{b}}\right) = \frac{\frac{\mathrm{d}\Psi_{\mathrm{up}}}{\mathrm{d}t} \cdot \frac{\mathrm{d}\Psi_{\mathrm{dw}}}{\mathrm{d}t}}{F_{\mathrm{sw}} \cdot \left(\frac{\mathrm{d}\Psi_{\mathrm{up}}}{\mathrm{d}t} - \frac{\mathrm{d}\Psi_{\mathrm{dw}}}{\mathrm{d}t}\right)} \tag{36}$$

To simplify the design of the circuital implementation of the fixed-frequency SMC, it is helpful to transform the practical control law, given in (30) and (31) as inclusive conditions, into the exclusive conditions given in (37) and (38) for both positive and negative transversality values, respectively.

$$\frac{\mathrm{d}}{\mathrm{d}u}\left(\frac{\mathrm{d}\Psi}{\mathrm{d}t}\right) > 0 \Rightarrow \left\{\begin{array}{lll} \text{if} \quad \Psi > \left.\dfrac{h\left(v_{\mathrm{pv}}, i_{\mathrm{pv}}, v_{\mathrm{b}}\right)}{2}\right|_{u=0} & \text{set} & \text{MOSFET OFF} \\ \text{if} \quad \Psi < -\left.\dfrac{h\left(v_{\mathrm{pv}}, i_{\mathrm{pv}}, v_{\mathrm{b}}\right)}{2}\right|_{u=1} & \text{set} & \text{MOSFET ON} \end{array}\right\} \tag{37}$$

$$\frac{\mathrm{d}}{\mathrm{d}u}\left(\frac{\mathrm{d}\Psi}{\mathrm{d}t}\right) < 0 \Rightarrow \left\{\begin{array}{lll} \text{if} \quad \Psi > \left.\dfrac{h\left(v_{\mathrm{pv}}, i_{\mathrm{pv}}, v_{\mathrm{b}}\right)}{2}\right|_{u=1} & \text{set} & \text{MOSFET ON} \\ \text{if} \quad \Psi < -\left.\dfrac{h\left(v_{\mathrm{pv}}, i_{\mathrm{pv}}, v_{\mathrm{b}}\right)}{2}\right|_{u=0} & \text{set} & \text{MOSFET OFF} \end{array}\right\} \tag{38}$$

Those control laws are implemented using two comparators, a Flip-Flop S-R and a digital microprocessor (or analog circuitry) to calculate $h\left(v_{\mathrm{pv}}, i_{\mathrm{pv}}, v_{\mathrm{b}}\right)$ online. Figures 9 and 10 show the electrical scheme of the proposed

Fig. 13 Response of the PV system with the SMC based on Ψ_L

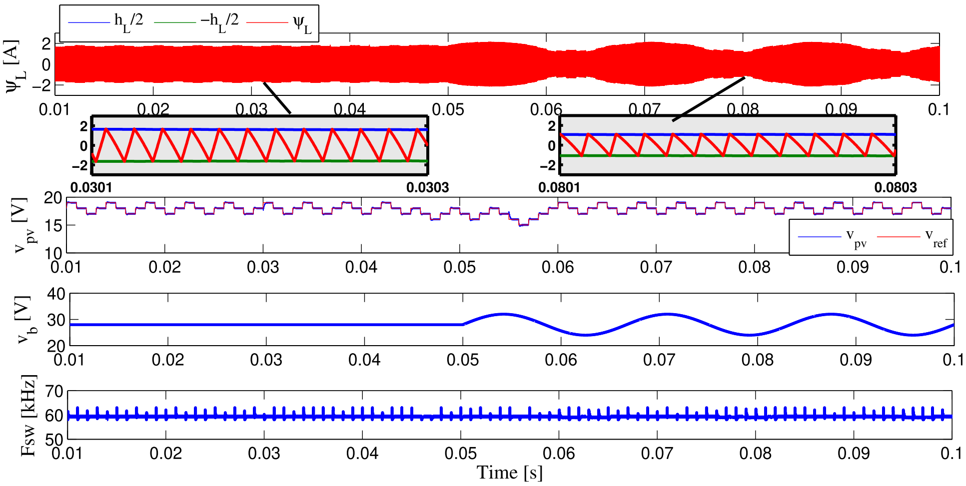

(a) Fixed-frequency implementation.

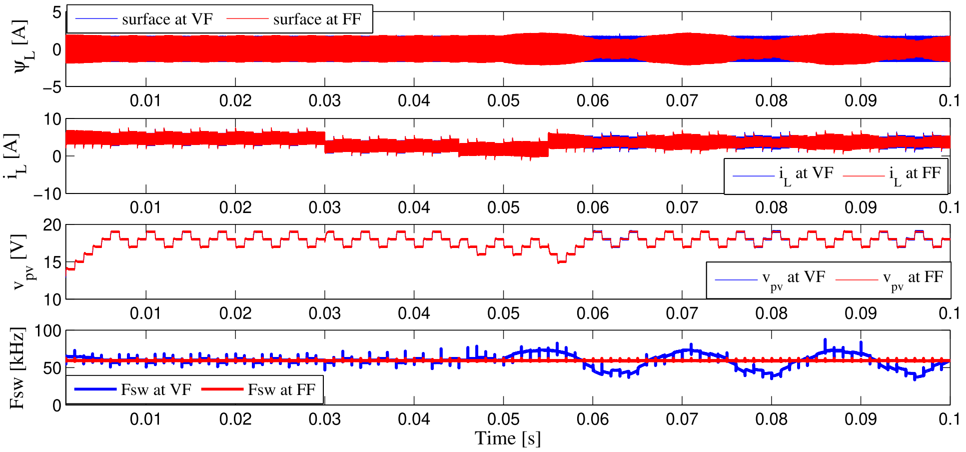

(b) Comparison of both fixed-frequency and variable-frequency implementations.

fixed-frequency implementation for SMC with both positive and negative transversality values, respectively. In such schemes it is assumed a digital microprocessor for calculating $h(v_{\mathrm{pv}}, i_{\mathrm{pv}}, v_{\mathrm{b}})$ since a wide range of commercial devices are available for this purpose. Moreover, such schemes can be also emulated in the power electronics simulator PSIM using a C block. In any case, analog circuitry could be also used, but such an implementation will require analog multipliers and dividers.

Application of the fixed-frequency implementation technique

This section illustrates the application of the proposed implementation technique using the three cases described in Sect. 2: inductor current control (case 1), input capacitor current control (case 2) and direct PV voltage control (case 3) for a grid-connected PV system.

The simulations of those SMC consider the following parameters: a BP585 PV module with parameters $A = 0.703\ \mathrm{V}^{-1}$ and $B = 0.894\ \mu\mathrm{A}$, a MPP voltage between 16.39 V and 18.13 V, a dc/dc converter with $L = 330$ uH and $C_{\mathrm{in}} = 22\ \mu\mathrm{F}$, an irradiance operation range from $S = 100\ \mathrm{W/m^2}$ to $S = 1000\ \mathrm{W/m^2}$, and a desired switching frequency $F_{\mathrm{sw}} = 60$ kHz.

The simulations of the implementation technique were performed using the power electronics simulation PSIM, and the calculation of $h(v_{\mathrm{pv}}, i_{\mathrm{pv}}, v_{\mathrm{b}})$ was implemented using C language. This procedure enables to tests the proposed solution by emulating the behavior of a Digital Signal Processor (DSP).

Case 1: inductor current control

The theoretical background of this SMC was previously described in Sect. 2.2. In this case, the explicit expression for calculating $h(v_{\mathrm{pv}}, i_{\mathrm{pv}}, v_{\mathrm{b}})$ is obtained by introducing the switching function derivatives (13) and (14) of Ψ_L into (36), obtaining (39). Such an expression must be calculated online by measuring v_{pv} and v_{b} as presented in Fig. 11, hence the ADC and DSP used for the implementation must to provide acquisition frequencies high enough, i.e., at least the double of the switching frequency [9].

$$h_L = \frac{v_{\mathrm{pv}}}{L \cdot F_{\mathrm{sw}}} \cdot \frac{v_{\mathrm{b}} - v_{\mathrm{pv}}}{v_{\mathrm{b}}} \tag{39}$$

Figure 12 presents the block diagram of the complete PV system including the fixed-frequency SMC. This block diagram implements the PV system equations (1), (2) and (3); moreover it follows the scheme depicted in Fig. 5 to include the MPPT algorithm. Taking into account the positive sign of the transversality for this case (12), the block diagram imposes the control law given in (37) following the circuital scheme described in Fig. 9. The block diagram also shows the C code used to calculate h_L as it is reported in (39).

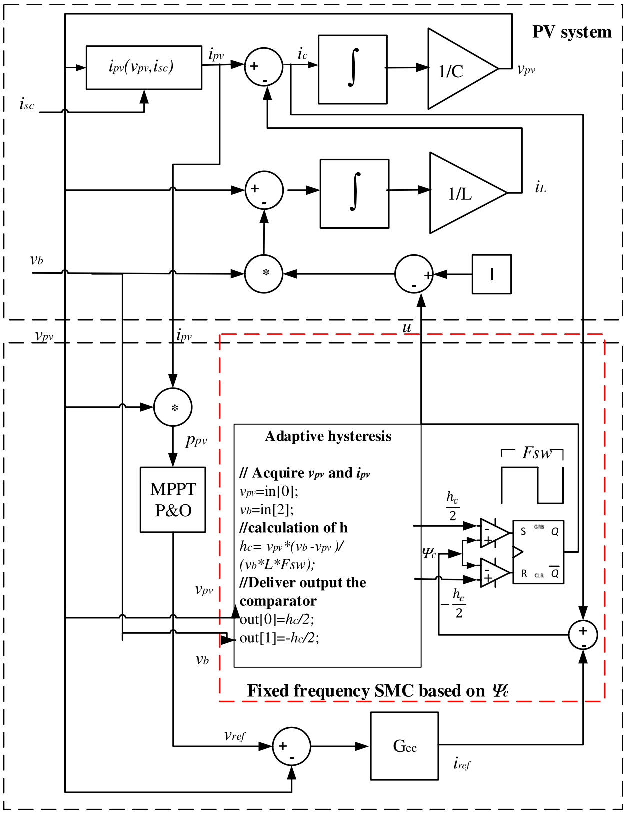

```
// Acquire vpv and ipv
vpv=in[0];
vb=in[2];
//calculation of h
hc= vpv*(vb -vpv )/
(vb*L*Fsw);
//Deliver output the
comparator
out[0]=hc/2;
out[1]=-hc/2;
```

Fig. 14 Block diagram of the SMC based on Ψ_C

The cascade voltage controller G_{cc} is designed using the transfer function given in (15), which is parameterized at the lower irradiance condition with $R_{\mathrm{MPP}} = 10\ \Omega$:

$$\frac{V_{\mathrm{pv}}(s)}{I_{\mathrm{ref}}(s)} = \frac{-10}{0.00022 \cdot s + 1} \tag{40}$$

The G_{cc} controller was designed with a PI structure, using the root-locus technique [26], based on the following criteria: a settling time of 0.9 ms and a damping ratio of 0.707, obtaining the controller given in (41).

$$G_{cc}(s) = -\frac{1.5 \cdot s + 1500}{s} \tag{41}$$

Figure 13a shows the electrical simulation the PV system, in which the size of the hysteresis band h_L is continuously adapted to keep the switching frequency constant at 60 kHz despite the presence of 30 % load voltage disturbances (v_{b}). The simulation uses a frequency meter to report the MOSFET switching frequency F_{sw}. Moreover, such a simulation shows the correct tracking of the reference provided by the

Fig. 15 Response of the system PV with the SMC based on Ψ_C

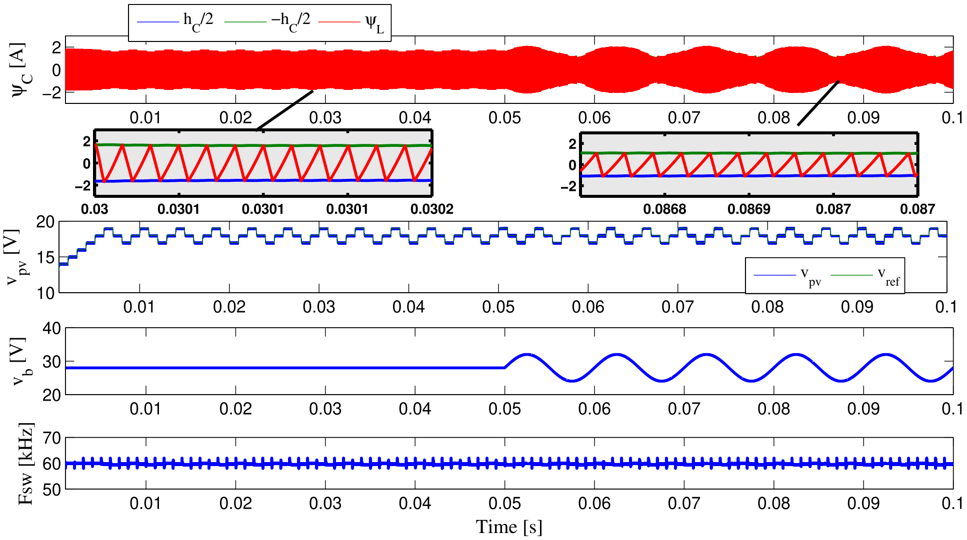

(a) Fixed-frequency implementation.

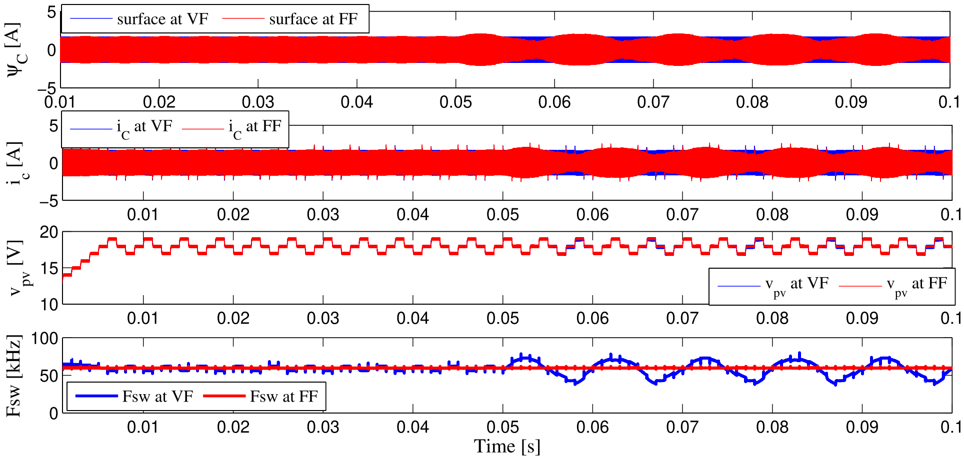

(b) Comparison of both fixed-frequency and variable-frequency implementations.

P&O algorithm, which enables the PV voltage to reach the optimal value that maximizes the generated power. In fact, an irradiance disturbance of 400 W/m^2 occurs at $t = 0.055$ s, but the cascade connection of the SMC, the PI controller and the P&O provide a satisfactory tracking of the new MPP. This fact is verified by the tree-point-behavior present in the PV voltage as it is reported in [14].

Figure 13b shows a comparison between both the classical (variable frequency) and the new fixed-frequency implementations of the same SMC based on Ψ_L. The difference between the hysteresis bands of both implementations for $t > 0.055$ s, when the disturbance in the load voltage takes place is noted. Similarly, the variation in the switching frequency of the classical solution, and the fixed frequency of the new solution, are evident. However, the performance of both solutions in tracking the optimal PV voltage is the same, i.e., both solutions reach the same optimal PV voltage (and power) at the same time. Therefore, the proposed fixed-frequency implementation ensures a constant switching frequency to the PV circuit without degrading the power production.

Case 2: capacitor current control

The theoretical background of this second SMC was described in Sect. 2.3. In this case, the explicit expression for calculating $h(v_{\mathrm{pv}}, i_{\mathrm{pv}}, v_{\mathrm{b}})$ is obtained by replacing (19) and (20) of Ψ_C into (36), obtaining (42).

$$h_{\mathrm{C}} = \frac{\left(\frac{\mathrm{d}i_{\mathrm{pv}}}{\mathrm{d}t} - \frac{v_{\mathrm{pv}}-v_{\mathrm{b}}}{L}\right)\cdot\left(\frac{\mathrm{d}i_{\mathrm{pv}}}{\mathrm{d}t} - \frac{v_{\mathrm{pv}}}{L}\right)}{F_{\mathrm{sw}}\cdot\left(\frac{v_{\mathrm{pv}}}{L} - \frac{v_{\mathrm{pv}}-v_{\mathrm{b}}}{L}\right)} \tag{42}$$

Analyzing the term $\frac{di_{\text{pv}}}{dt}$ requires to derive expression (3) as follows:

$$\frac{di_{\text{pv}}}{dt} = \frac{di_{\text{SC}}}{dt} - B \cdot A \cdot \frac{dv_{\text{pv}}}{dt} \cdot e^{A \cdot v_{\text{pv}}} \tag{43}$$

Replacing the differential equation (2) into (43):

$$\frac{di_{\text{pv}}}{dt} = \frac{di_{\text{SC}}}{dt} - B \cdot A \cdot e^{A \cdot v_{\text{pv}}} \left(\frac{i_{\text{pv}} - i_L}{C_{\text{in}}} \right) \tag{44}$$

In [16] was demonstrated that the equilibrium point of the SMC is defined by $\left\{ i_{\text{pv}} = i_L \right\}$; moreover the derivative of the short-circuit current, caused by the natural change in the irradiance, is very small in comparison with the derivative of the inductor current as it is discussed in [17]. Therefore, approximating $\frac{di_{\text{SC}}}{dt} \approx 0$ does not introduce significant errors in the framework of the switching frequency. Under the light of those considerations, equation (44) ensures that $\frac{di_{\text{pv}}}{dt} \approx 0$ holds, which leads to the following expression for the adaptive hysteresis band:

$$h_C = \frac{v_{\text{pv}}}{L \cdot F_{\text{sw}}} \cdot \frac{v_{\text{b}} - v_{\text{pv}}}{v_{\text{b}}} \tag{45}$$

The relations within the state-space model reported in Sect 2.3 are illustrated in the block diagram of Fig. 14. Moreover, since the transversality of the SMC based on Ψ_C has a negative sign, the control law given in (38) is implemented using the circuital scheme described in Fig. 10. In this case the cascade voltage controller is designed using a parameterized version of (22); which enables to design, by means of the root-locus method, the proportional controller given in (46) to provide a constant settling time equal to 0.2 ms.

$$G_{cc}(s) = 0.44 \tag{46}$$

Figure 15a shows the simulation of the fixed-frequency implementation, which provides a satisfactory tracking of the optimal operation condition and a constant switching frequency of 60 kHz: the three-point behavior of the PV voltage ensures the P&O algorithm has detected the MPP, hence the PV system is producing the maximum power. Moreover, from $t = 0.05$ s the load voltage exhibits a 30 % disturbance, which is compensated by the adaptive hysteresis band to provide a constant frequency. Figure 15(b) shows a comparison between both fixed-frequency and variable-frequency implementations of the same SMC based on Ψ_C, where the difference in the hysteresis band under v_{b} disturbances is evident. The figure also put into evidence the variable-frequency operation caused by the classical implementation due to changes in the operating point, which is not the case for the new fixed-frequency solution. However, both solutions reach the same optimal operation condition at the same time, hence the proposed fixed-frequency implementation provides the same performance in comparison with the classical (variable-frequency) approach.

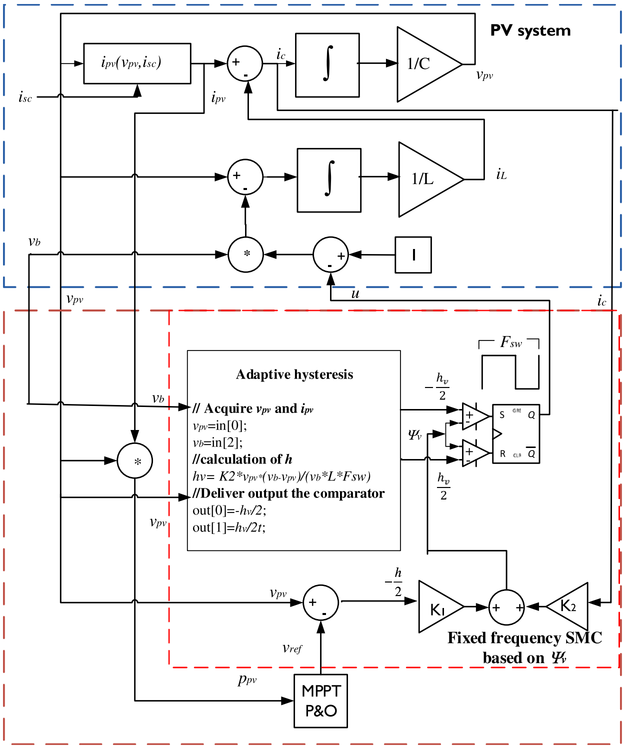

```
// Acquire vpv and ipv
vpv=in[0];
vb=in[2];
//calculation of h
hv= K2*vpv*(vb-vpv)/(vb*L*Fsw)
//Deliver output the comparator
out[0]=-hv/2;
out[1]=hv/2t;
```

Fig. 16 Block diagram of the SMC based on Ψ_V

Case 3: direct PV voltage

A summary of the theoretical background of this case is given in Sect. 2.4, while a complete description of the equations and analyses for the SMC based on Ψ_V is available in [9]. In this third case, the calculation of $h\left(v_{\text{pv}}, i_{\text{pv}}, v_{\text{b}}\right)$ is based on (25) and (26) assuming i_{SC} is almost constant within the switching period, which has a negligible impact as it was discussed in the previous subsection. Moreover, to simplify expressions (25) and (26) it is safe to assume an almost constant voltage reference v_{ref} provided by the P&O algorithm, which does not introduce significant errors because v_{ref} has a square-like waveform, hence it only presents changes in a very short time. Finally, it is assumed that the SMC imposes a correct tracking of the reference, hence the behavior of v_{pv} follows the behavior of v_{ref}. Those assumptions are formalized as $\frac{di_{\text{SC}}}{dt} = 0$ and $\frac{dv_{\text{pv}}}{dt} = \frac{dv_{\text{ref}}}{dt} = 0$, which provide the following simplified versions of (25) and (26):

Fig. 17 Response of the system PV with the SMC based on Ψ_V

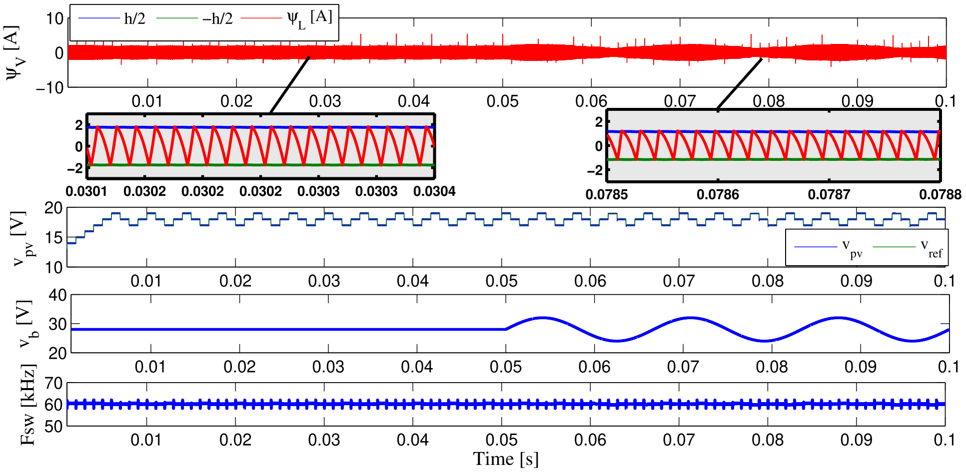

(a) Fixed-frequency implementation.

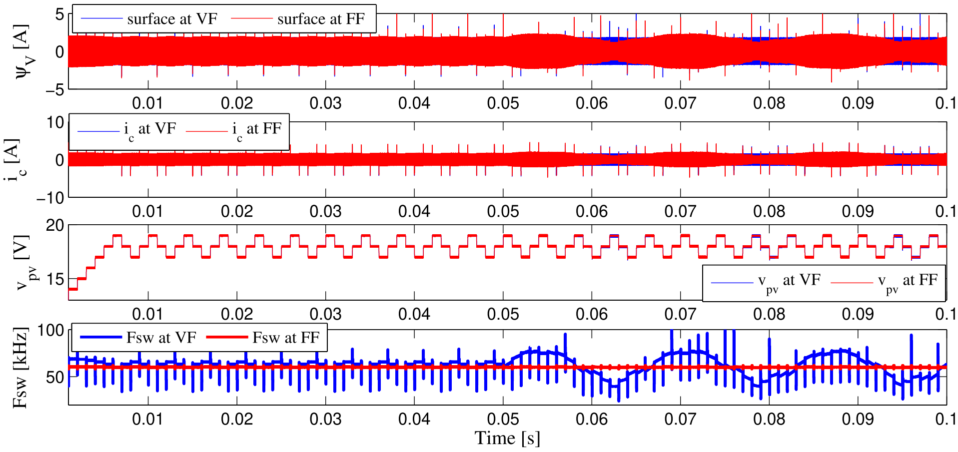

(b) Comparison of both fixed-frequency and variable-frequency implementations.

$$\lim_{\Psi \to 0^-} \left. \frac{d\Psi_V}{\mathrm{d}t} \right|_{u=1} = -K_2 \cdot \frac{v_{\mathrm{pv}}}{L} > 0 \tag{47}$$

$$\lim_{\Psi \to 0^+} \left. \frac{d\Psi_V}{\mathrm{d}t} \right|_{u=1} = -\frac{K_2 \cdot v_{\mathrm{pv}} - v_{\mathrm{b}}}{L} < 0 \tag{48}$$

The expression for the adaptive hysteresis h_V, for this case, is obtained by replacing both (47) and (48) into (36):

$$h_V = \frac{K_2 \cdot v_{\mathrm{pv}} \cdot (v_{\mathrm{pv}} - v_{\mathrm{b}})}{F_{\mathrm{sw}} \cdot L \cdot v_{\mathrm{b}}} \tag{49}$$

Taking into account the positive sign of the transversality for this case, relations between the state-space equations given in Sect. 2.4, and the adaptive hysteresis (49), are illustrated in the block diagram of Fig. 16.

Figure 17(a) shows the simulation of the SMC based on Ψ_V implemented with the proposed fixed-frequency technique. As in the previous cases, the implementation circuit provides a constant switching frequency (60 kHz) even under load disturbances of 30 % and, at the same time, it ensures a three-point behavior in the PV voltage. Therefore, the PV system is driven to produce the maximum power possible. Figure 17(b) shows the comparison of both fixed-frequency and variable-frequency implementations, where both solutions have the same performance in the tracking of the optimal operation condition. Hence, as in the previous cases, the new implementation technique provides a constant switching frequency without degrading the power production.

Experimental validation

This section presents the experimental validation of the proposed implementation methodology. The proof-of-concept prototype reported in Fig. 18 enables to validate the performance of the fixed-frequency implementations of Case 1 and Case 3. In particular, Fig. 18a describes the prototype setup. The selected PV panel is a BP585 module, while the dc-link and the grid-connected inverter are emulated using a four quadrant electronic source/load BOP 50-20GL from Kepco. Such a device enables to implement the sinusoidal voltage disturbances considered in the simulation. Moreover, a P&O MPPT algorithm was designed with $\Delta v_{\mathrm{pv}} = 1\,V$ and $T_{\mathrm{a}} = 0.1\,s$ following the procedure reported in [14]. The implemented surfaces Ψ, the adaptive hysteresis and the MPPT algorithm are calculated using a DSP F28335 controlCARD from Texas Instruments and converted to analog voltages with a DAC MCP4822; those signals are provided to the SMC Analog circuit. In addition, the switching circuits of Figs. 9 and 10 are implemented with a set of amplifiers, comparators and a TS555 integrated circuit as it is explained in [9]. The hysteresis comparators are implemented to enable the modification of the analog value h, which provides the variable-switching circuit presented in Fig. 9. Moreover, an amplification circuit is used to scale Ψ to the required TS555 offset. Subsequently, the binary control signal u is generated by the TS555, which is provided to the MOSFET driver A3120.

The boost dc/dc converter is implemented using a 2218-H-RC inductor from Bourns Inc with $L = 330\ \mu H$, two MKT1813622016 capacitors from Vishay BC with $C = 22\ \mu F$ for C_{in} and C_{b}, and two IRF540N MOSFETs from International Rectifier. In addition, the inductor and the input capacitor currents are measured using shunt-resistors $R_{\mathrm{s}} = 5\ m\Omega$ and AD8210 amplifiers. Those current and voltage measurements are acquired by the DSP using the onboard ADCs. Finally, the physical setup of the experimental platform is shown in Fig. 18b, where the PV module, the dc/dc converter, the DSP and the SMC analog circuit are observed.

The solution is evaluated with two experiments; the first one validates the proposed implementation technique with the positive transversality SMC based on Ψ_L (Case 1), while the second experiment validates the proposed implementation technique with the negative transversality SMC based on Ψ_V (Case 3).

In the first experiment, the SMC based on Ψ_L was programed into the DSP. A comparison between both the variable-frequency and the fixed-frequency implementations of the SMC is reported in Fig. 19, which is in agreement with the simulation results previously presented in Fig. 13. The experimental validation illustrates in Fig. 19a the performance of the classical approach, which exhibits frequency variations when the disturbance in the load voltage occurs. The frequency variation is observed in the signal density of Ψ: higher density means higher frequency and viceversa. The switching frequency measurement provided by the oscilloscope in this experiment is always changing, hence it is not provided in the figure.

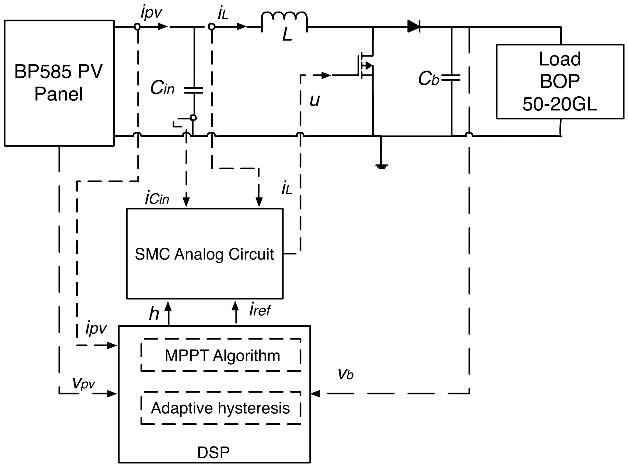

(a) Electrical scheme

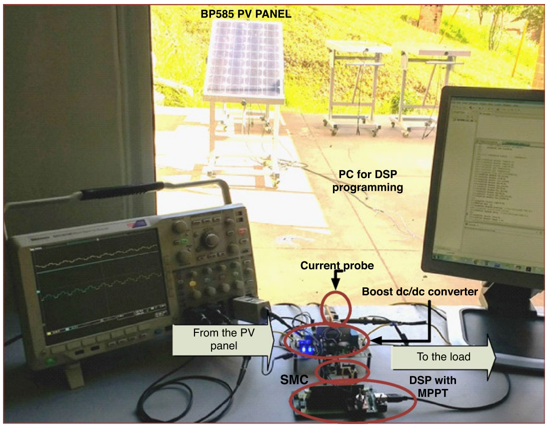

(b) Physical setup

Fig. 18 Experimental platform

In contrast, Fig. 19b presents the validation of the fixed-frequency implementation, which provides the three-point behavior of the PV voltage and a constant switching frequency of 59.78 kHz, which is a 0.36 % error with respect to the desired switching frequency of 60 kHz. In addition, this experiment shows the hysteresis band is adapted to compensate the load disturbances and to avoid changes in the switching frequency. Comparing the experimental results given in Fig. 19a, b it is noted that both solutions reach the same optimal PV voltage, hence the proposed fixed-frequency implementation provides the same performance, in terms of power production, in comparison with the classical variable-frequency approach. In conclusion, the results of this first experiment puts into evidence the satisfactory performance of the proposed solution to guarantee a fixed switching frequency to the SMC.

The second set of experiments considers the implementation of the SMC based on Ψ_V presented in Case 3. Similar to the previous validation, the experimental platform was evaluated considering the comparison between both

Fig. 19 Experimental implementations of Case 1

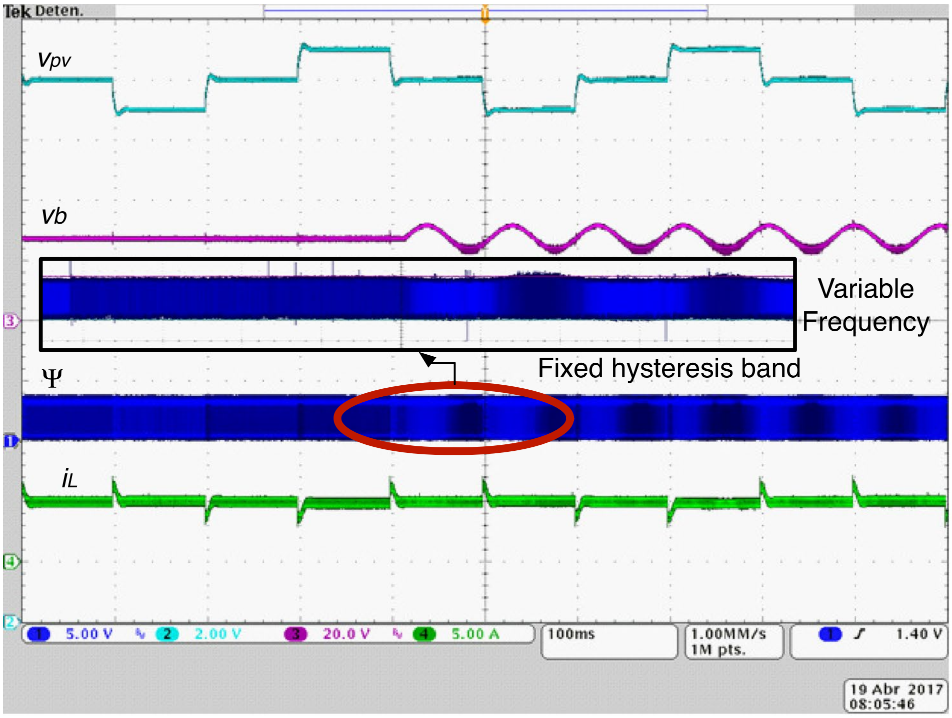

(a) Variable-frequency SMC test with Ψ_L

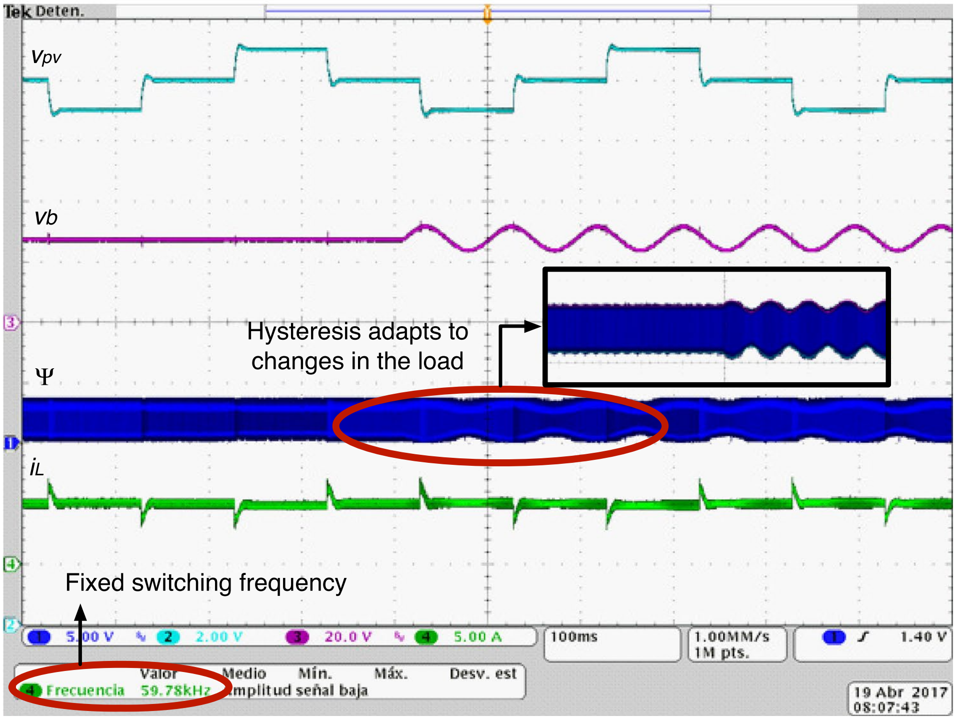

(b) Fixed-frequency SMC test with Ψ_L

the variable-frequency and the fixed-frequency implementations shown in Fig. 20. The variable-frequency implementation, based on a fixed hysteresis band, is evaluated in Fig. 20a. In that experiment the PV system is producing the maximum power (denoted by the three-point behavior), but the switching frequency is not constant when the load disturbances are present. Figure 20b shows the fixed-frequency implementation, which ensures a constant switching frequency of 60.65 kHz, hence a 1.08 % error with respect to the desired switching frequency of 60 kHz,

Fig. 20 Experimental implementations of Case 3

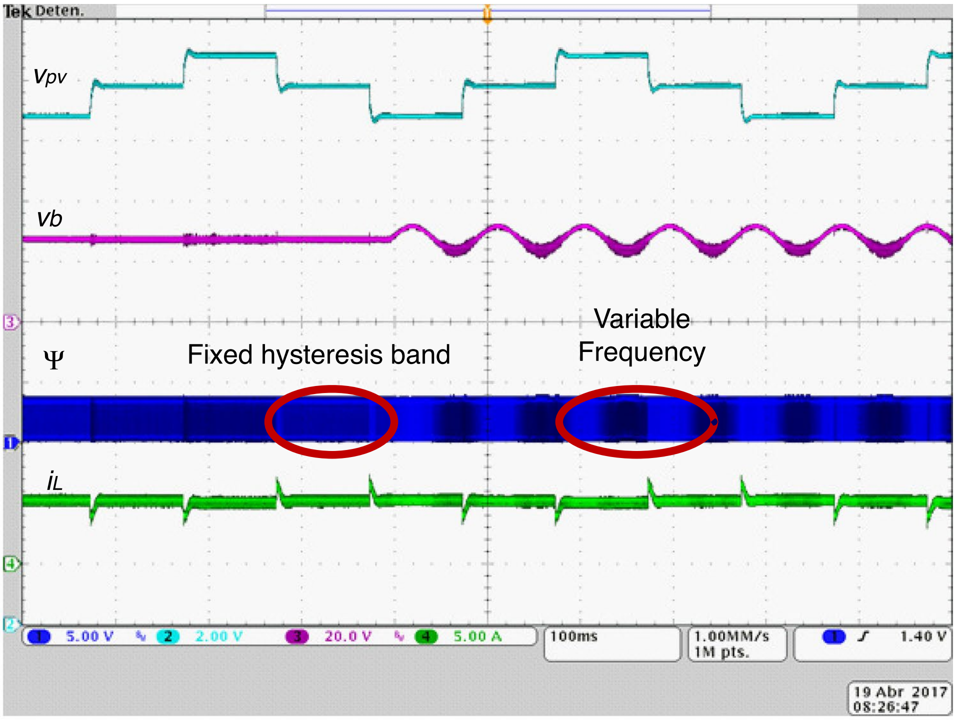

(a) Variable-frequency SMC test with Ψ_V

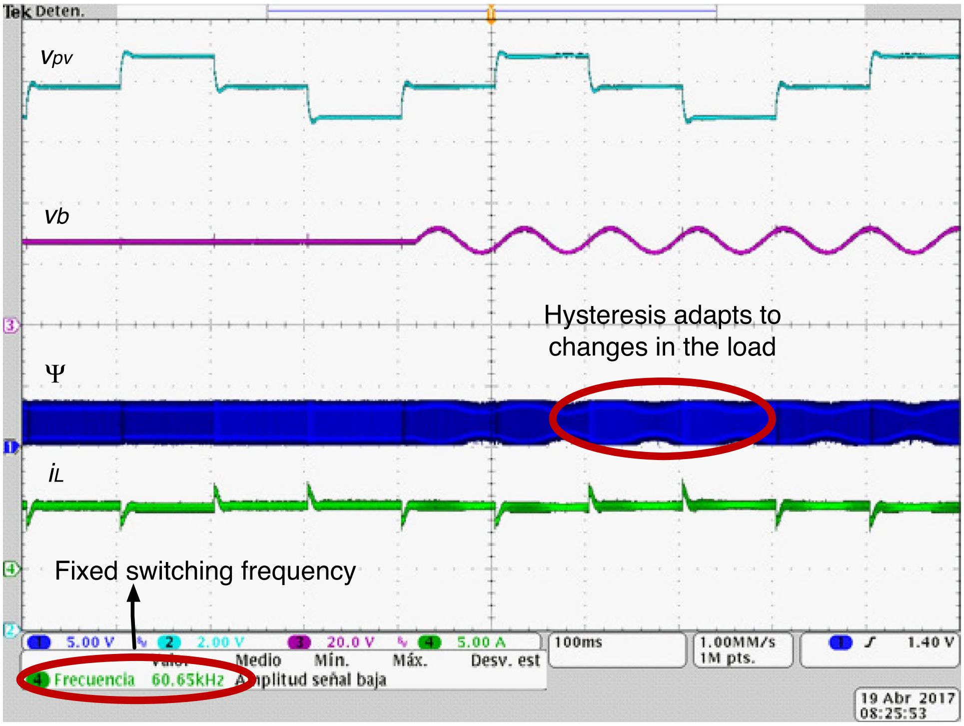

(b) Fixed-frequency SMC test with Ψ_V

without degrading the PV power production. Therefore, this second set of experiments shows the effectiveness of the proposed solution also in the implementations of SMC with direct regulation of the PV voltage.

Finally, the experimental results presented in this section demonstrate the correctness of the proposed fixed-frequency implementation for SMC applied to PV systems, in both positive and negative transversality cases.

Conclusions

This paper has presented a novel implementation methodology for sliding-mode controllers featuring constant switching frequency, which is aimed for SMC applied to photovoltaic systems. The proposed solution does not affect the performance of the SMC, hence there is no difference in the power produced by the PV system in comparison with the classical implementation based on variable frequency. Such a performance was validated using both detailed simulations and experimental measurements on a real prototype under different atmospheric conditions and load disturbances.

Therefore, the proposed fixed-frequency implementation methodology enables to precisely design filters for removing the switching noise from current and voltage signals, and to design the elements of the dc/dc converter without accounting for a worst-case scenario as in the case of variable frequency. However, this method is only applicable to SMC based on first-order surfaces, which limits the control systems able to be implemented of this solution. In any case, a large amount of PV systems are based on first-order surfaces, as it was discussed in the paper.

Finally, the proposed methodology could be extended to enable the implementation of high-order surfaces, e.g., maximum power point tracking strategies based on nonlinear equations. Such an approach will require to extend the equations used to calculate the dynamic hysteresis band depending on each particular surface. This work is under development to increase the spectrum of sliding-mode controllers able to be implemented with the proposed solution.

Acknowledgements This work was supported by the Automatic, Electronic and Computer Science research group of the Instituto Tecnológico Metropolitano, the Universidad Nacional de Colombia and Colciencias (Fondo Nacional de Financiamiento para la Ciencia, la Tecnología y la Innovación Francisco José de Caldas) under the doctoral scholarship 2012-567 and the projects UNAL-ITM-39823/P17211 and "Estrategia de transformación del sector energético Colombiano en el horizonte de 2030 - Energetica 2030" - "Generación distribuida de energía eléctrica en Colombia a partir de energía solar y eólica" (Code: 58838, Hermes: 38945).

References

1. Petrone, G., Spagnuolo, G., Teodorescu, R., Veerachary, M., Vitelli, M.: Reliability issues in photovoltaic power processing systems. IEEE Trans. Ind. Electron. **55**(7), 2569 (2008)
2. Hernandez, J.C., Bueno, P.G., Sanchez-Sutil, F.: Enhanced utility-scale photovoltaic units with frequency support functions and dynamic grid support for transmission systems. IET Renew. Power Gener. **11**(3), 361 (2017)
3. Jurasz, J., Ciapała, B.: Integrating photovoltaics into energy systems by using a run-off-river power plant with pondage to smooth energy exchange with the power gird. Appl. Energy **198**, 21 (2017)
4. Bueno, P.G., Hernandez, J.C., Ruiz-Rodriguez, F.J.: Stability assessment for transmission systems with large utility-scale photovoltaic units. IET Renew. Power Gener. **10**(5), 584 (2016)
5. Hernandez, J.C., Garcia, O.G., Jurado, F.: Photovoltaic devices under partial shading conditions. Int. Rev. Model. Simul. **5**(1), 414 (2012)
6. Spagnuolo, G., Petrone, G., Lehman, B., Ramos Paja, C.A., Zhao, Y., Orozco Gutierrez, M.L.: Control of photovoltaic arrays: dynamical reconfiguration for fighting mismatched conditions and meeting load requests. IEEE Ind. Electron. Mag. **9**(1), 62 (2015)
7. Romero-Cadaval, E., Spagnuolo, G., Franquelo, L.G., Ramos-Paja, C.A., Suntio, T., Xiao, W.M.: Grid-connected photovoltaic generation plants: components and operation. IEEE Ind. Electron. Mag. **7**(3), 6 (2013)
8. Femia, N., Lisi, G., Petrone, G., Spagnuolo, G., Vitelli, M.: Distributed maximum power point tracking of photovoltaic arrays: Novel approach and system analysis. IEEE Trans. Ind. Electron. **55**(7), 2610 (2008)
9. Gonzalez, D., Ramos-Paja, C.A., Giral, R.: Improved design of sliding mode controllers based on the requirements of mppt techniques. IEEE Trans. Power Electron. **31**(1), 235 (2016)
10. Femia, N., Petrone, G., Spagnuolo, G., Vitelli, M.: A technique for improving p&o mppt performances of double-stage grid-connected photovoltaic systems. IEEE Trans. Ind. Electron. **56**(11), 4473 (2009)
11. Trejos, A., Gonzalez, D., Ramos-Paja, C.A.: Modeling of step-up grid-connected photovoltaic systems for control purposes. Energies **5**(6), 1900 (2012)
12. Khanna, R., Zhang, Q., Stanchina, W., Reed, G., Mao, Z.H.: Maximum power point tracking using model reference adaptive control. IEEE Trans. Power Electron. **29**(3), 1490 (2014)
13. Dounis, A.I., Kofinas, P., Alafodimos, C., Tseles, D.: Adaptive fuzzy gain scheduling pid controller for maximum power point tracking of photovoltaic system. Renew. Energy **60**, 202 (2013)
14. Femia, N., Petrone, G., Spagnuolo, G., Vitelli, M.: Optimization of perturb and observe maximum power point tracking method. IEEE Trans. Power Electron. **20**(4), 963 (2005)
15. Bianconi, E., Calvente, J., Giral, R., Mamarelis, E., Petrone, G., Ramos-Paja, C.A., Spagnuolo, G., Vitelli, M.: Perturb and observe mppt algorithm with a current controller based on the sliding mode. Int. J. Electr. Power Energy Syst. **44**(1), 346 (2013)
16. Bianconi, E., Calvente, J., Giral, R., Mamarelis, E., Petrone, G., Ramos-Paja, C.A., Spagnuolo, G., Vitelli, M.: A fast current-based mppt technique employing sliding mode control. IEEE Trans. Ind. Electron. **60**(3), 1168 (2013)
17. Ortiz Valencia, P.A., Ramos-Paja, C.A.: Sliding-mode controller for maximum power point tracking in grid-connected photovoltaic systems. Energies **8**(11), 12363 (2015)
18. Alsumiri, M.A., Jiang, L., Tang, W.H.: Maximum power point tracking controller for photovoltaic system using sliding mode control. In: IET Conference Publications, vol. 2014, (2014)
19. Gonzalez Montoya, D., Ramos Paja, C.A., Giral, R.: Maximum power point tracking of photovoltaic systems based on the sliding mode control of the module admittance. Electr. Power Syst. Res. **136**, 125 (2016)
20. Levron, Y., Shmilovitz, D.: Maximum power point tracking employing sliding mode control. IEEE Trans. Circuits Syst. I Regul. Pap. **60**(3), 724 (2013)

21. He, Y., Luo, F.: Sliding-mode control for dc/dc converters with constant switching frequency. IEE Proc. Control Theory Appl. **153**(1), 37 (2006)
22. Tan, S., Lai, Y.M., Tse, C.K.: General design issues of sliding-mode controllers in dc-dc converters. IEEE Trans. Ind. Electron. **55**(3), 1160 (2008)
23. Li, B., Guo, S., Lin-Shi, X., Allard, B.: Design and implementation of the digital controller for boost converter based on fpga. In: 2011 IEEE International Symposium on Industrial Electronics, pp. 1549–1554, (2011)
24. Utkin, V., Lee, H.: Chattering problem in sliding mode control systems. In: 2nd IFAC Conf. on Analysis and Design of Hybrid Systems (Alghero, Italy), pp. 7–9, (2006)
25. Sahu, P.K., Mahakhuda, R.K., Maity, S., Maity, S.: A fixed switching frequency sliding mode control for single-phase voltage source inverter. In: International Conference on Circuit, Power and Computing Technologies [ICCPCT], pp. 1006–1010, (2014)
26. Petrone, G., Ramos-Paja, C.A., Spagnuolo, G.: Photovoltaic Sources Modeling. Wiley, New York (2017)
27. Sira-Ramirez, H.: Sliding motions in bilinear switched networks. IEEE Trans. Circ. Syst. **CAS–34**(8), 919 (1987)